COMMUNICATION

Entirely Flexible On-Site Conditioned Magnetic Sensorics

Niko Münzenrieder, Daniil Karnaushenko,* Luisa Petti, Giuseppe Cantarella, Christian Vogt, Lars Büthe, Dmitriy D. Karnaushenko, Oliver G. Schmidt, Denys Makarov,* and Gerhard Tröster*

Flexible electronics[1–4] naturally conform to static or dynamically reconfigurable complex 3D shaped surfaces[5,6] offering intimate yet durable contact with biological as well as synthetic tissues. The inherent feature of this new concept of electronics of being soft and compliant enables a plethora of new applications. Especially the fields of medical[7] and consumer electronics[8] benefit from the variety of already available flexible devices including electrode arrays,[9,10] solar cells,[11] diagnostic devices,[12–15] displays,[16] memory elements,[17,18] and various types of sensors.[19–24]

At the moment, postprocessing, e.g., signal amplification, or multiplexing of the data acquired by *entirely flexible* and even *imperceptible* devices,[5,25–28] such as pressure,[11,29,30] temperature,[26,30] encephalography,[7,27] or magnetic field[22,24,25] sensors, is done using external rigid electronics. The connection between the flexible and the rigid parts of the measurement system is established using cables. This measurement scheme—although commonly applied to condition flexible sensors—limits the unobtrusiveness, narrows the system bandwidth, and possesses strong disadvantages in terms of signal-to-noise ratio (SNR). In particular, the poor noise performance is due to the simultaneous amplification of the signals and the noise, which is either picked up upon the signal transmission using long cables, or produced by power supplies and electronic circuits itself. To enhance the responsiveness and sensitivity of an acquisition system, the output of a sensory system should be amplified directly at the sensor location. This so called frontend sensor signal conditioning is a standard approach in conventional rigid microelectronics but is not yet established for flexible electronics.[26,31]

Here, we demonstrate a fully integrated yet entirely flexible magnetosensory system, which can be fabricated over large areas (**Figure 1**a–d). The complete system (Figure 1e–f) is integrated on a single 50 µm thick polyimide foil and consists of a differential giant magnetoresistive (GMR) sensing element arranged in a Wheatstone bridge configuration (Figure 1g), an operational amplifier with differential high impedance input and single ended output, based on 16 indium–gallium–zinc–oxide (IGZO) thin-film transistors (TFTs)[2] (Figure 1e and **Figure 2**a, inset), and a high current output amplifier TFT operated as class A power amplifier with an open drain output to provide maximum adaptability to different loads (Figures 1e and 2b, inset). The differential and power amplifier readout circuitry remains fully operational and reveals remarkable amplification of 48.6 dB also at high frequencies with a unity gain frequency of about 200 kHz resulting in a gain-bandwidth product of 54 MHz even while bent to a radius of 5 mm. The readout circuitry is designed to operate in the digital or analog regime and is able to convert a low voltage differential signal (LVDS) such as switching square shaped signals into larger voltage single-ended responses for data transmission or control operations. Furthermore, the analog differential signaling promotes an efficient rejection of common mode noises (achieved by an internal common mode rejection feedback) leading to an extremely low noise floor of –124 dBm Hz^{-1}. The presented work demonstrates for the first time that IGZO semiconductor devices enable the realization of entirely flexible low-noise electronics, suitable for sensor readout circuits. To achieve a high as possible SNR, the flexible GMR elements were arranged in a Wheatstone bridge configuration. The flexible GMR bridge possesses remarkable advantages compared to individual flexible sensor elements.[12,22,24,25,32,33] In particular, their differential output connected to the input of the differential operational amplifier allows processing of small signals in the microvolts range and efficiently rejects common mode noise acquired from external disturbances and power lines.

Dr. N. Münzenrieder
Sensor Technology Research Center
University of Sussex
Falmer, Brighton BN1 9QT, UK
E-mail: n.s.munzenrieder@sussex.ac.uk
Dr. N. Münzenrieder, L. Petti, G. Cantarella, C. Vogt, L. Büthe, Prof. G. Tröster
Electronics Laboratory
ETH Zürich
8092 Zürich, Switzerland
D. Karnaushenko, D. D. Karnaushenko, Prof. O. G. Schmidt, Dr. D. Makarov
Institute for Integrative Nanosciences
Institute for Solid State and Materials Research Dresden (IFW Dresden)
01069 Dresden, Germany
E-mail: d.karnaushenko@ifw-dresden.de; d.makarov@hzdr.de
Prof. O. G. Schmidt
Material Systems for Nanoelectronics
Chemnitz University of Technology
09107 Chemnitz, Germany
Prof. O. G. Schmidt
Center for Advancing Electronics Dresden
Dresden University of Technology
01062 Dresden, Germany
Dr. D. Makarov
Helmholtz-Zentrum Dresden-Rossendorf
Institute of Ion Beam Physics and Materials Research
01328 Dresden, Germany

DOI: 10.1002/aelm.201600188

ADVANCED ELECTRONIC MATERIALS
www.advelectronicmat.de

Materials Views
www.MaterialsViews.com

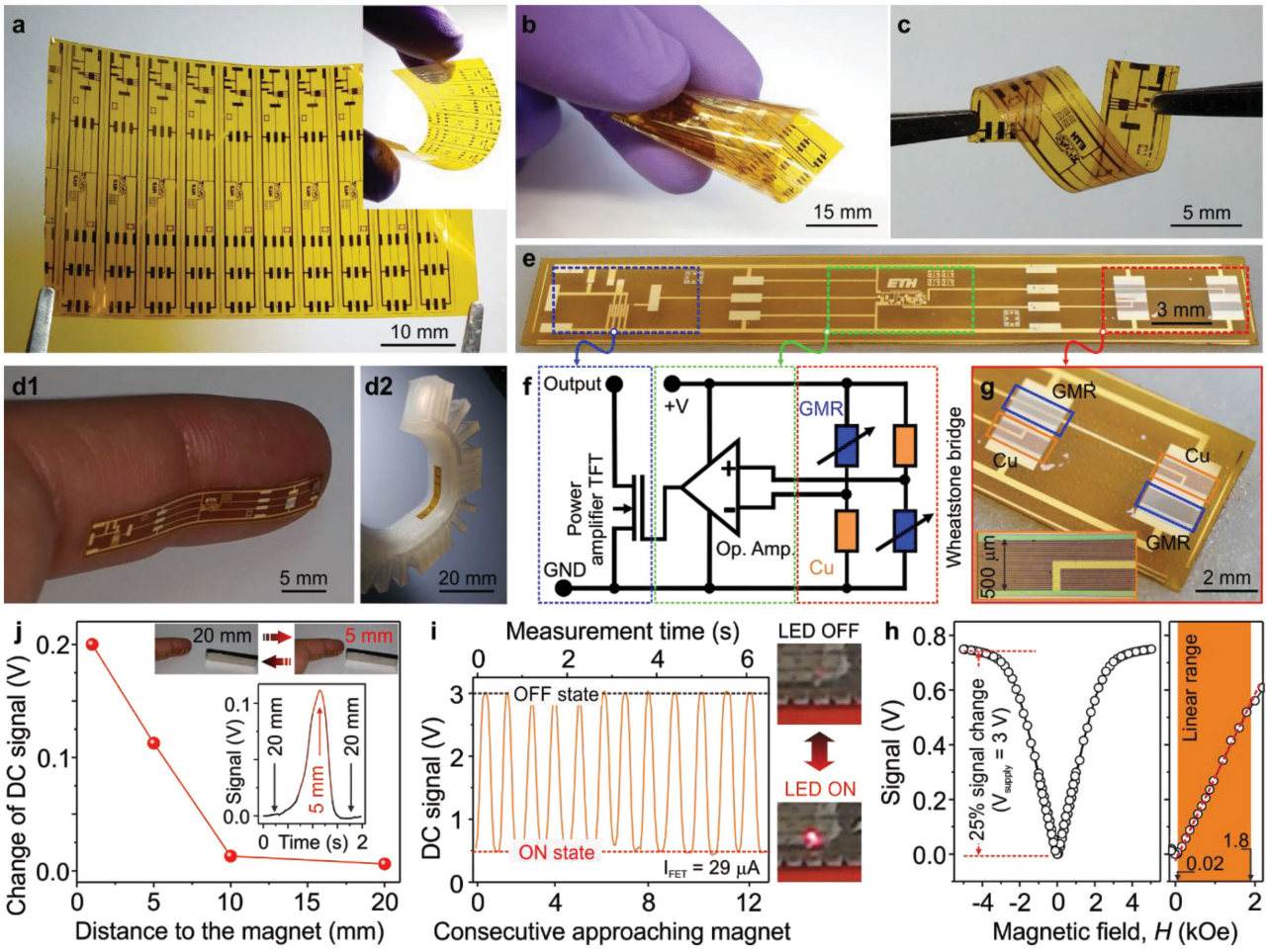

Figure 1. a) Array of flexible magnetosensory systems. The systems can be bent (b,c) or located on curved surfaces (d). These flexible magnetosensitive sensors can be used to monitor displacements or motion and provide feedback as needed, e.g., for smart implants, and proximity sensorics for on-skin or wearable electronics (d1) but also to realize the sensory feedback for a unique class of soft actuators—soft robotics (d2). The complete system (e,f) is fabricated on a single 50 µm thick polyimide foil and consists of an operational amplifier, an output power amplifier and GMR elements arranged in a Wheatstone bridge configuration (g). Each resistor in the bridge possesses a meander shape (inset in panel (g)). h) Magnetoresistive response of the magnetic sensor bridge with respect to the external magnetic field. The region where the sensor reveals linear response is indicated in orange. i) Flexible magnetic switch: output signal of the system exposed to a magnetic field of a permanent magnet, here the magnet is periodically approaching the location of the sensor bridge. The performance of the device is sufficient to trigger the ON/OFF state of a commercial LED. j) Flexible magnetic proximity sensor for on-skin applications: response of the system recorded while approaching a permanent magnet. In this case, the signal is measured directly at the output of the operational amplifier.

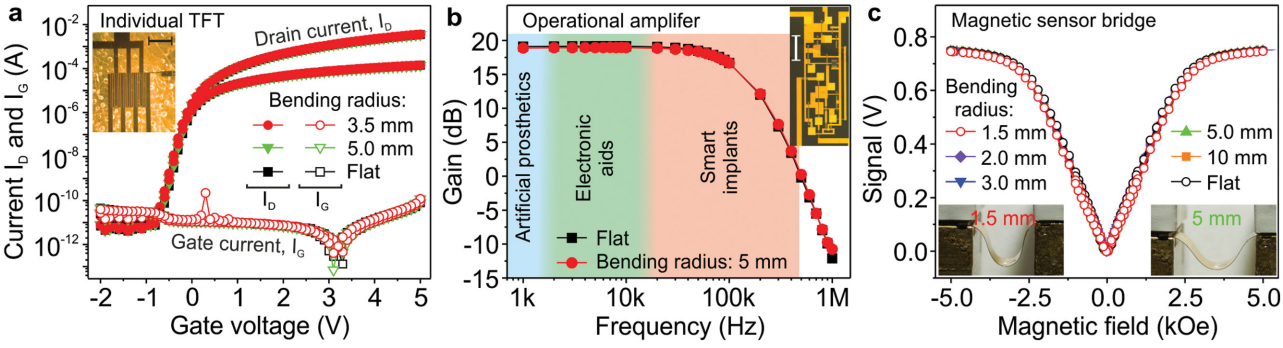

Figure 2. a) Transfer characteristics of an IGZO power transistor measured in the linear (V_{DS} = 0.1 V) and saturation (V_{DS} = 5 V) regime while flat and bent. Scale bar in the inset is 500 µm. b) Bode plot of the operational amplifier in planar and bent state (without power amplifier), and application examples operating at frequencies within the bandwidth of the flexible amplifier. The inset shows the operational amplifier (scale bar is 500 µm). c) Response of the magnetic sensor bridge (without readout circuitry) measured at different bending radii and plotted versus applied magnetic field.

Table 1. Comparison of state-of-the-art magnetic field sensor solutions. "n.a." stands for not applicable; "n.p."—for not provided; "GMI"—for giant magnetoimpedance: and "SQUID-VSM"—for superconducting quantum interference device - vibrating sample magnetometer.

	Resp. sensor [V kOe^{-1}] Resp. integrated [V V^{-1} kOe^{-1}] Linear range [|Oe| ÷ |Oe|]	Operating voltage [V]	Power cons. [mW]	Band width 3 dB [kHz]	Noise floor $f > 100$ Hz [dBm Hz^{-1}]	Rigid/flexible
GMR sensor[51]	3 [V] n.p. 1.5 ÷ 10	<|±25|	≈1	>1000	n.p.	Rigid
GMR sensor[52]	1.2 [V] n.p. 0 ÷ 10	1.2 ÷ 9	50	>1000	−186	Rigid
Hall sensor[53]	n.p. 9 0 ÷ 90	2.5 ÷ 38	6.75 ÷ 102	20	−84	Rigid
GMI sensor[54]	n.p. 10^5 0 ÷ 0.0004	5	75	0.1 ÷ 1	−76	Rigid
SQUID-VSM[55]	n.p. n.p. 0 ÷ 70000	230 ÷ 380	10^7	1 ÷ 10	−196	Rigid
GMI sensor[56]	0.045 [mA] n.a. 0 ÷ 1	n.a.	n.a.	n.p.	n.p.	Flexible Min. bending radius: 30 µm
GMI sensor[19]	n.p. n.a. 0 ÷ 5	n.a.	n.a.	n.p.	n.p.	Flexible Min. bending radius: 72 mm
GMR sensor[57]	0.0025 [mA] n.a. 500 ÷ 2000	n.a.	n.a.	n.p.	n.p.	Flexible Min. bending radius: 12 mm
GMR sensor[25]	0.004 [mA] n.a. 50 ÷ 200	n.a.	n.a.	n.p.	n.p.	Flexible Min. bending radius: 3 µm
GMR sensor[32] in an external rigid bridge	4 [V] n.a. 50 ÷ 200	0.01 of sensor + lock-in 220	0.01 of sensor + lock-in 100 W	<100	−121 after lock-in	Flexible Min. bending radius: 2 mm
GMR bridge [this work]	0.08 [V] 53 50 ÷ 3000	1.7 ÷ 5	0.25	<100	−124	Flexible Min. bending radius: 5 mm

For demonstration purposes, the differential IGZO-based operational amplifier and the class A output power amplifier are integrated with the magnetic sensor bridge. The on-site amplification of the bridge output within the flexible sensor system results in a high responsiveness of 25 V V^{-1} kOe^{-1} owing to the high total gain of 48.6 dB of the flexible readout circuitry. This corresponds to a 270 times enhancement of the signal amplitude, which is the highest gain of flexible amplifiers reported so far (Table 2). With these parameters, the *mechanically flexible magnetosensory system* outperforms its rigid commercially available counterparts (**Table 1**). Operating at only 3 V supply, the open drain output enables the use of high and low impedance loads and can reach a full scale amplitude with an output current of up to 3 mA (Figure 2a) suggesting the possibility to directly drive external power demanding devices such as a relay or light emitting diodes (LEDs). Besides its high current driving capability, the device consumes less than 250 µW at 1.7 V and 450 µW at 3 V (1 MΩ load), rendering the circuit the most power efficient entirely flexible fully integrated sensory system reported so far (Table 1).[34–37] This remarkable energy efficiency potentially allows the system to be powered using renewable green energy sources, e.g., flexible energy harvesters and storage elements.[38–41] We envision that the integrated GMR bridge can be used to trigger external devices or provide feedback signals paving the way toward the realization of entirely flexible magnetic gadgets and switches. These components are needed for interactive consumer electronics, e.g., *intelligent* packaging, postcards, or promotional materials in the spirit of the internet of things (IoT) concept. Furthermore, the device bandwidth is appropriate to cover a broad range of sensor applications, e.g., for prosthetics, implants, and monitoring appliances integrated into biological and artificial structures. Especially, devices operating at frequencies bellow 100 kHz require low noise switches and sensory feedback (Figure 2b). Therefore, integrated flexible magnetosensitive devices can be used to monitor displacements or motion and provide feedback as needed, e.g., for smart implants,[42] body worn ultrasound navigation system (20–200 kHz),[43] acoustic virtual reality for visually impaired people (20 kHz),[44] wound monitoring systems (1 mHz–1 kHz),[45] proximity sensorics for on-skin or wearable electronics (Figure 1d1),[46] or for the realization of actively controlled soft actuators[47–50] (Figure 1d2).

The central element of the flexible high-performance integrated magnetosensitive system is a differential n-channel metal–oxide–semiconductor field-effect transistor (NMOS) operational amplifier based on 16 bottom-gate inverted staggered IGZO thin-film transistors (details on preparation are in the Experimental Section). IGZO-based electronics[2,18,35,58–62] has been chosen for its high-performance and low power operation. In particular a carrier mobility beyond 10 cm^2 V^{-1} s^{-1} and extreme bending

ADVANCED ELECTRONIC MATERIALS
www.advelectronicmat.de

Materials Views
www.MaterialsViews.com

radii down to the micrometer range[5,23] render IGZO an attractive alternative to organic semiconductor-based devices.[26,31,63–66]

The operational amplifier circuit (Figures 1e,f and 2b) consists of a differential stage with a common mode rejection feedback, a dual to single ended converter, and an additional common source output stage exhibiting an amplification of 19 dB and a common mode rejection ratio of 44 dB.[58] In addition, two current sources (current mirrors) are included to enable circuit operation without external bias voltages. The used IGZO TFTs also ensures a very high input impedance of >10 GΩ. The output of the operational amplifier is connected to a high current output TFT (Figures 1e,f and 2a) forming an open drain circuit acting as class A power amplifier. The output can be directly connected to an external device, which has to be triggered.

To assess the electrical performance of the flexible two-stage amplifier, the input of the operational amplifier is subjected to differential 3 Hz sinusoidal and 3 kHz square wave signals with peak-to-peak amplitudes of 10 and 250 mV, respectively (**Figure 3**). Here the circuit input is biased to a DC offset of 1.5 V in order to operate within the allowed common mode input range, and to imitate the output signal of the GMR bridge. The conditioned single-ended operational amplifier output signal is then applied to the input of the output power amplifier (Figure 1e,f), whereas the high current TFT is biased to 15 µA using an external source. This output power amplifier is formed by an individual high current TFT exhibiting a transconductance up to 1.4 mS and a transit frequency of 200 kHz. By monitoring the intermediate output signal of the operational amplifier and the overall output of the readout

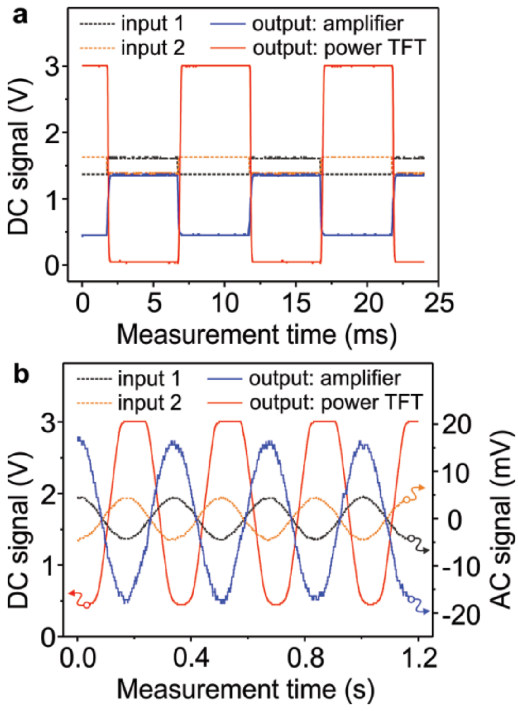

Figure 3. Intermediate response of the operational amplifier (blue) and overall output of the readout electronics (red) on an externally applied square wave (a) and sinusoidal (b) differential input signals. The data reveal a total open loop gain of 48.6 dB, whereas the supply voltage was 3 V and the oscilloscope (1 MΩ) was used as a load element.

electronics for the square (sinusoidal) input signals a output signal amplitude of ≈1 V (40 mV) and 3 V (2.7 V) is measured, respectively (Figure 3a,b). Here the gain of the larger square wave input signal is limited by the supply voltage.

Operating in the digital regime, the flexible device is able to switch on or off an external commercial LED at only ±250 mV of applied differential square input signal (Figure 1i). With this performance, the circuit can serve as a differential-input-single-ended-output buffer (with high input and low output impedance) to convert data from the LVDS domain into a single-ended high voltage signal. In the analog mode, the gain reaches values as high as 48.6 dB (Figure 3), which is crucial for sensory applications where an as high as possible amplification is required, e.g., position encoders of mechanical systems. In order to drive a commercial LED directly connected to the output (Movie S1, Supporting Information), the amplitude of a differential sinusoidal input signal is increased to 250 mV to enhance the current amplitude at the output. When 3 V is supplied to the device, it consumes only 550 µW while powering a commercial LED chip (Movie S2, Supporting Information).

The noise performance of the flexible circuitry is characterized by measuring the frequency dependence of the noise spectral density at ambient conditions with a 50 Ω load resistor connected to the output of the readout circuit. Here, a standard 50 Ω load was inserted between the power TFT drain electrode and the 3 V power line. A differential signal source (output impedance 50 Ω) was connected to the circuit input, and the noise characteristic was measured while the source was switched off, and a differential sinusoidal signal with 10 µV peak-to-peak amplitude was applied. The frequency of the sinusoidal signal was set to 15 kHz, well below the cutoff frequency of the circuit. The data (**Figure 4**a) reveal a noise floor of the circuit of −124 dBm Hz^{-1} at frequencies above 100 Hz, where the contribution from the 1/f noise is negligible. This value corresponds to a signal of about 400 nV $Hz^{-1/2}$ (peak to peak). Furthermore, the remarkably low noise floor assures a large signal-to-noise ratio of at least 56 dB (Figure 4b), and the high sensitivity better than −112 dBm Hz^{-1} of the flexible readout circuit (defined as the minimum input power spectral density needed to produce an output signal with a SNR of 56 dB). With these characteristics, the flexible circuit is suitable for the demonstrated fully integrated flexible magnetosensitive sensor system carrying a frontend amplifier for differential signals from a GMR Wheatstone bridge and an output power amplifier.

Here, we report the very first realization of flexible GMR Wheatstone bridges. The GMR Wheatstone bridge is fabricated on the same substrate as the IGZO circuitry and connected to the differential high impedance input of the flexible operational amplifier. The GMR bridge consists of two reference nonmagnetic Cu-based resistors and two magnetoresistive elements (Figure 1e–g) implemented by giant magnetoresistive Co/Cu multilayer stacks coupled in the first antiferromagnetic maximum.[33,67–69] Each magnetic field sensor reveals a magnetoresistive effect of 25% (change of the signal is 0.75 V at the supply voltage of 3 V, Figure 1h). The responsivity of the GMR bridge reaches a value of 84 mV V^{-1} kOe^{-1}. The saturation field of the GMR elements is tuned to be ≈5 kOe to ensure linear response in a broad field range from 20 Oe to about 1.8 kOe (Figures 1h and 2c) as required for proximity sensing in a variety of applica-

ADVANCED ELECTRONIC MATERIALS
www.advelectronicmat.de

COMMUNICATION

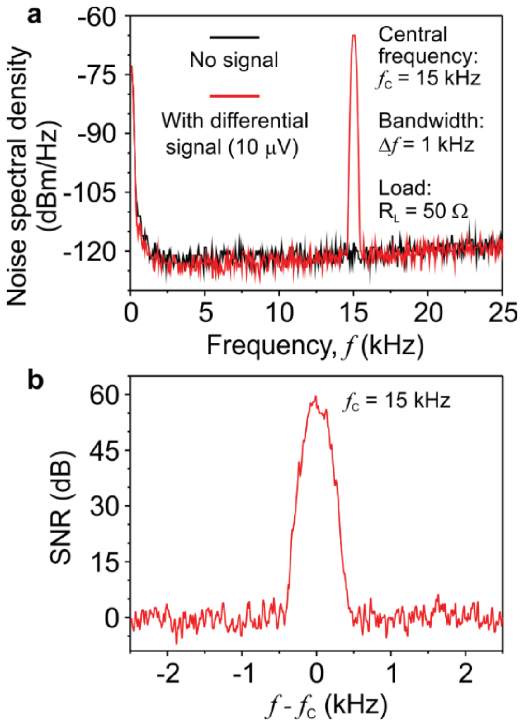

Figure 4. a) Noise floor of the readout circuitry circuit (–124 dBm Hz^{-1}) measured at the output of the power amplifier without (black) and with (red) a small differential sinusoidal signal (10 μV peak-to-peak voltage and frequency of 15 kHz) applied at the input of the operational amplifier. Bandwidth is 1 kHz. The GMR bridge is not connected. b) Magnified spectral density demonstrating the SNR of 56 dB.

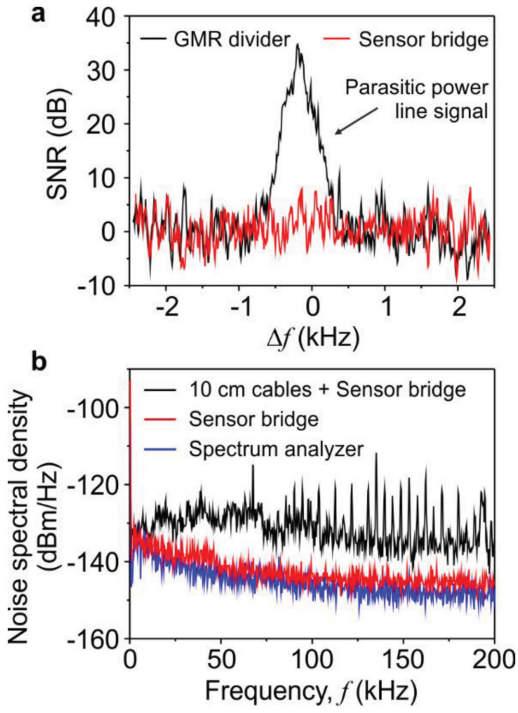

Figure 5. a) Common mode noise measured at the GMR divider (black) and at the Wheatstone bridge terminals (red). The sensor bridge is powered using a switching power supply producing disturbances in the power line (central frequency: 102.5 kHz). As visible from the graph, these disturbances are efficiently suppressed by the differential signal processing. b) Noise figure of the magnetic sensor bridge connected via 10 cm long not-shielded cables (black) demonstrating severe disturbances induces in the cables acting as antennas. Noise spectral density measured directly at the magnetic sensor bridge (red), revealing a noise floor very close to those of the spectrum analyzer used for characterization (blue). The bandwidth of the spectrum analyzer was set to 1 kHz.

tions including feedback sensory systems for robotics or consumer electronics.

The Wheatstone bridge offers strong advantages over the single sensor elements in terms of temperature and electrical stability. The small differential signals (84 mV V^{-1} kOe^{-1}) obtained from the GMR bridge in response to an external magnetic field are amplified by the integrated operational amplifier. The output power amplifier additionally amplifies the signal. Thereby, the total responsiveness of the devices is approaching 25 V V^{-1} kOe^{-1}, which is at least one order of magnitude higher than commercial fully integrated rigid magnetic sensors (Table 1). Compared to the measurement data obtained from individual GMR sensor elements common mode noise is efficiently rejected, and low noise operation is possible when using the GMR bridge (**Figure 5**a) in combination with the differential operational amplifier. The demonstrated frontend detection and amplification is an important feature to enhance the sensitivity of the sensor system. The bridge output, measured directly at the amplifier input, reveals a total noise of less than –145 dBm Hz^{-1} (corresponds to the noise of the spectrum analyzer used to characterize flexible devices).

For comparison, a traditional setup where the signal has to be transmitted through cables to reach the rigid readout electronics was simulated by measuring the noise figure after passing the sensor signal through 10 cm long cables. The measured noise level of –120 dBm Hz^{-1} reveals that the integrated system approach presented here results in a more than 25 dBm Hz^{-1} signal-to-noise level improvement. Without the integrated amplifier, all the disturbances (Figure 5b) acquired by long cables (as in an antenna) would be amplified by an external circuit resulting in the strong suppression of the electrical performance of the system.

The high current TFT forming the output power amplifier stays fully operational while bent to a radius of 3.5 mm and exhibits only small DC parameter changes such as a threshold voltage reduction of –25 mV and an increase of the effective mobility by 1% (Figure 2a). The operational amplifier is also tested under bending to a radius of 5 mm revealing a voltage gain of 18.9 dB, a –3 dB frequency of 113 kHz, a unity gain frequency of 508 kHz, and unchanged common mode rejection. Hence, the operational amplifier possesses the gain-bandwidth product (GBWP) of 4.48 MHz (Figure 2b). The gain-bandwidth product of the complete readout circuitry is 54 MHz and a signal gain 48.6 dB, which is the highest value reported for the entirely flexible thin film amplifiers (**Table 2**).

The GMR characteristics, namely the GMR magnitude and the responsiveness of the sensor bridge, remain unchanged even when the sample is bent down to a radius of 1.5 mm (Figure 2c). The bridge was powered by 3 V using an external power supply and the magnetoelectric characterization was

Table 2. Comparison of state-of-the-art flexible amplifiers. "n.p." stands for not provided.

	Circuit type	Operating voltage [V]	DC power consumption [mW]	Gain [dB]	−3 dB bandwidth [kHz]	Unity gain frequency [kHz]	GBWP [MHz]	Rigid/flexible
Self-aligned IGZO TFT[62]	Common source	5	n.p.	6	n.p.	3200	6.4	Flexible Min. bending radius: 5 mm
Organic TFT[70]	Operational amplifier	15	0.225	20	<0.03	2	0.02	Flexible Min. bending radius: n.p
IGZO TFT[71]	Operational amplifier	6	6.78	19	25	330	2.9	Flexible Min. bending radius: n.p.
IGZO TFT[72]	Cascode	6	1.5	31	252	≈3500	124	Flexible Min. bending radius: n.p.
Crystalline Si ribbons[73]	Operational amplifier	n.p.	n.p.	4	≈100	≈100	0.16	Flexible Min. bending radius: 6 mm
IGZO TFT[58]	Operational amplifier	5	0.9	18.7	108	472	4.1	Flexible Min. bending radius: 5 mm
IGZO TFT[5]	Differential pair	12	n.p.	≈2.2	≈2000	≈2000	2.6	Flexible Min. bending radius: 50 μm
This work	Operational amplifier (with power output amplifier)	1.7	0.25	48.6	≈113	>200	54	Flexible Min. bending radius: 5 mm

performed in an electromagnet in a configuration where the magnetic field was parallel to the bridge plane.

With this remarkable performance, the integrated magnetosensory system offers vast possibilities in detection of motion or can operate as a magnetically activated energy efficient sensor and switch. These operation modes are highlighted using the following demonstrators.

Switching electrical devices between on and off states is the most explored application field of conventional rigid magnetic field sensorics used, e.g., as light bulb trigger in refrigerators, or closure state detectors of a roof window in a car. Although flexible,[22,57,74] stretchable,[25,33,68] and even printable[57,75,76] magnetic field sensorics have already been developed, entirely flexible high-performance fully integrated magnetic switches have not been realized yet.[75,76]

For this demonstrator, we prepared an extra flexible circuit consisting of an IGZO TFT and a commercial semiconductor light emitting diode connected to the drain of the TFT using printed silver electrodes. The external LED circuit is fixed in a probe station and supplied with 3 V using an external power supply. The flexible magnetic sensory system is subjected to 1.7 V supply. The output power amplifier is biased to a current of 15 μA, and its output is connected to the gate electrode of the external TFT acting as switching element for the LED. The GMR bridge is approached with an external permanent NdFeB magnet and signals are acquired by a multichannel oscilloscope connected to the output of the operational amplifier, the drain of the high current TFT, and the drain of the external TFT. The readout circuitry converts the differential sensor signal from the GMR bridge into a single-ended signal, varying between two discrete output voltage levels of 0 and 1.7 V (Movie S3.1, Supporting Information). The system reveals a full-scale output signal (Figure 1i and Movie S3.2, Supporting Information) in response to a small magnetic field of only 40 Oe. This output signal is used to drive the external TFT resulting in the manipulation of the on/off state of the LED. The entire flexible circuit without LED is powered at 1.7 V consuming only ≈250 μW, which allows its autonomous work when supplied by available flexible energy harvesting or storage elements.[38–40]

We envision that these magnetic switches will be highly relevant in medicine for applications where mechanical flexibility, light weight and energy efficiency of the electronic components are of major relevance, e.g., heart pacemaker, brain implants, hearing aids, capsule endoscopes, mechanical prosthetics, health threat alarming devices, or automatic delivery systems. In this respect, thin flexible fully integrated switches that are triggered by an external magnetic field or a small permanent magnet could reduce size and power consumption of the final wearable devices or smart implants.

Proximity sensor operation mode: Linear magnetic field sensors are an important component in any automated mechanical system where position control of mechanical parts is required. Robotics, e.g., mechanical prosthetics is a prominent example of such kind of system. If successfully fabricated, mechanically flexible linear magnetic field sensorics would enable the realization of a feedback systems for entirely flexible mechanical parts[77,78] including soft actuators[79] and soft robotics[47] (Figure 1d2).

We demonstrate that the developed flexible magnetic sensor system can be used as a linear proximity sensor to detect the distance or the spatial location of a magnet. The GMR bridge is approached with an external permanent NdFeB magnet (field at the surface of the magnet is 3 kOe) and signals are acquired by a multichannel oscilloscope connected to the output of the operational amplifier, and the overall output of the readout circuit. Additionally, the flexible external LED circuit is connected to the sensor system. The entire setup consumes 550 μW (450 μW without the LED) and is powered using an external power supply providing 3 V. The distance from the GMR bridge

to the magnet is visualized by monitoring the light intensity of a commercial LED (Movie S4, Supporting Information). Furthermore, the output signal of the sensor system can be correlated to the distance between magnet and GMR bridge (Figure 1j). The magnet can already be detected at a distance of 20 mm.

In conclusion, we realized the first entirely flexible integrated magnetic field sensor system hosted on a 50 µm thin polyimide foil. The system consists of a flexible giant magnetoresistive bridge on-site conditioned using high-performance IGZO-based electronic devices. The differential output of the magnetic sensor bridge is connected to the high input impedance differential input of the flexible operational amplifier composed of 16 IGZO TFTs. The amplifier converts the differential input into a single ended output signal and exhibits a gain of about 19 dB. An additional high current output stage configured as class A power amplifier with open drain connection boosts the overall gain of the readout electronics to the record high value of 48.6 dB. In addition to the remarkably high gain of the readout electronics, the sensitivity of the system strongly benefits from the high signal-to-noise ratio of 56 dB. The demonstrated system is able to detect magnetic fields with a sensitivity of 25 V V^{-1} kOe^{-1} and thus outperforms the responsiveness of commercial fully integrated rigid magnetic sensors by at least one order of magnitude, whereas all components stay fully functional when bend to a radius of 5 mm. Our high-performance flexible magnetosensory system represents a key step toward entirely flexible electronics, capable of sensing, and processing signals without the need of rigid elements.

We outlined potential application directions of the developed system in monitoring displacements or motion and providing feedback as needed, e.g., for smart implants, body worn ultrasound navigation system, acoustic virtual reality for visually impaired people, proximity sensorics for on-skin or wearable electronics and for the realization of actively controlled soft actuators. In this respect, two demonstrators are realized, namely magnetic switch and proximity sensing device with remarkably low power consumption of down to 250 µW even when used to trigger an external LED. The achieved energy efficiency allows the autonomous work of the system when using available flexible energy harvesting or storage elements.

Experimental Section

Fabrication of IGZO Circuitry: The devices are manufactured on free-standing 50 µm thick polyimide substrate using a layer stack which is reported in refs. [58] and [60]. Prior to the fabrication, the polyimide foil was cleaned with acetone and isopropyl alcohol, preshrunk at 200 °C to remove trapped residual solvents and finally encapsulated with 50 nm SiN_x using a plasma-enhanced chemical vapour deposition (PECVD) process. The SiN_x barrier layers increase the adhesion, and improve the dimensional stability of the substrate by reducing the abortion of liquids, and therefore swelling processes during the fabrication process. The subsequent amplifier fabrication is based on NMOS design using bottom-gate inverted staggered and passivated IGZO TFTs. Layer structuring is done using standard UV lithography in combination with wet etching and lift-off processes. The device fabrication starts with the evaporation and structuring of 35 nm thick Cr bottom gates and interconnection lines, which are afterward electrically insulated by a 25 nm thick Al_2O_3 film (dielectric constant of ≈9.5), prepared using atomic layer deposition. The semiconducting amorphous IGZO (15 nm thick) is deposited by radio frequency (RF) magnetron sputtering using an InGaZnO target with a stoichiometric composition of In:Ga:Zn:O = 1:1:1:4. After the structuring of the IGZO and Al_2O_3 layers, a 10 nm thick Ti adhesion layer and a 60 nm thick Au film are evaporated and structured into source/drain contacts, interconnection lines and contact pads by lift-off process. An additional layer of 25 nm Al_2O_3 is used to passivate the TFT back channels. The fabrication process is optimized concerning low temperature fabrication (maximum process temperature: 150 °C) as well as adhesion and thickness of different material layers aiming at electrical performance, long term reliability and bendability. The flexible TFTs are fabricated with a minimum feature size of 6 µm.

Fabrication of GMR Bridge: Before the fabrication of the magnetic sensors, all IGZO-based devices were protected with novel photo patternable polychloroprene. The photosensitive polymer is prepared from a mixture of polychloroprene (0.75 g) in 25 mL of 3 parts (v/v) cyclopentanone and 1 part (v/v) 1-methoxy-2-propanole, following 50 mg of 2-benzyl-2-(dimethylamino)-4-morpholinobutyrophenone and 150 mg of pentaerythritol triacrylate are added to the mixture. The solution was stirred for 2 h and then spin coated at 6000 rpm for 35 s resulting in a layer thickness of 100 nm. The sample is exposed to 405 nm mercury h-line (20 mW cm^2) for 1.5 min through a glass/Cr mask in a SUSS MA4 mask aligner. Development is done by washing the sample in 4-methyl-2-pentanone for 5 s. All chemicals were purchased from Sigma-Aldrich Co. LLC. We note that the polymeric encapsulation appeared to be vital to achieve functional devices. The attempt to electrically insulate electronics using the 25 nm thin Al_2O_3 passivation layer prepared using atomic layer deposition failed due to the existence of pinholes in the Al_2O_3 on the millimetre sized sensor area.

The Wheatstone bridge is composed of four resistors. One pair are trilayer Co(1 nm)/Cu(26 nm)/Co(1 nm) reference resistors. Those are designed to balance the second pair of magnetosensitive elements consisting of 80 bilayers of Co(1 nm)/Cu(1.2 nm) prepared on 1 nm thick Co buffer layer. The 1 nm thick bottom Co film is used to improve the adhesion of thin metal films to the flexible Polyimide foils. When exposed to atmosphere, the top 1 nm thick Co film forms a dense CoO oxide layer, which acts as a self-passivating layer protecting all resistors of the Wheatstone bridge from further oxidation. The metal thin-films are prepared at room temperature via magnetron sputter deposition in a high-vacuum chamber (base pressure: 7.9×10^{-7} mbar; Ar sputter pressure: 9.4×10^{-4} mbar; deposition rate: 0.2 Å s^{-1}). All resistors are patterned as meanders using combination of photolithography and shadow masks. A positive UV lithography lift-off process is performed using AZ 5214E resist (AZ electronic materials) and a SUSS MA4 mask aligner. Each meander contains 12 turns with line width of 10 µm and the total length of 38 mm. The footprint of each resistor in the Wheatstone bridge is 1.5×1.0 mm^2. Since the differential amplifier has a high input impedance, the geometry of the meander is optimized to achieve a comparably large sensor resistance of about 7.7 kΩ. This results in the reduction of the current flowing through the bridge and improves the power efficiency of the sensor system.

Characterization of the GMR Bridge: The individual GMR sensor element is characterized at room temperature by locating the sensor between the pole shoes of an electromagnet. The magnetic field is applied in the sensor plane and the change of the electrical resistance is measured in a two-point configuration as a function of the applied magnetic field. The GMR ratio is defined as the magnetic field dependent change of the sample's resistance, $R(H_{ext})$, normalized to the resistance value of the magnetically saturated sample, R_{sat}: $GMR(H_{ext}) = [R(H_{ext}) - R_{sat}]/R_{sat}$. For the samples used in this study, a GMR effect of 25% is experimentally determined. The slope of the linear part of the GMR curve represents the field responsiveness of the GMR bridge, which is found to be 84 mV V^{-1} kOe^{-1}.

The GMR performance, namely the GMR magnitude and the GMR responsiveness, remains unchanged even when the sample is bent down to a radius of 1.5 mm (Figure 2c). Bending experiments are carried out using a computer controlled motorized stage, which is placed in between the poles of an electromagnet.[25,80] For the bending tests the samples were aligned to apply lateral stress and clamped in the

motorized stage (insets in Figure 2c). The distance between the clamps is successively reduced to bend the samples. The magnetoresistance is measured in the central region, where the curvature is most pronounced. The bending radii between the two central contacts are evaluated using calibrated photographs and image processing software. The obtained values exhibit an uncertainty of 3%.

The differential electrical performance was characterized using a spectrum analyzer in three different configurations (Figure 2b). Here the noise spectral density was measured with (I) the disconnected (50 Ω loaded) spectrum analyzer, (II) the spectrum analyzer directly connected to the differential output of the powered GMR bridge, and (III) the spectrum analyzer connected to the bridge using 10 cm long signal cables. The measured signal shows that a direct connection of the amplifier to the bridge is required in order to enhance the signal-to-noise ratio. Additionally, an efficient common mode noise rejection (Figure 4a) of the bridge compared to a single ended sensor is demonstrated.

Characterization of the Electrical Properties of IGZO Devices: Single transistors and complete operational amplifiers are characterized under ambient conditions. Typical IGZO TFT performance parameters extracted from transfer characteristics using the Shichman Hodges model are as follows: field effect mobility ≈11 $cm^2\ V^{-1}\ s^{-1}$, threshold voltage ≈0.2 V, subthreshold swing ≈140 mV dec^{-1}, and on/off current ratio $>10^6$. Furthermore, the shortest fabricated TFT exhibits a transit frequency of ≈12 MHz, extracted from s-parameter measurements using a network analyzer and low noise ground-signal-ground probe tips.

The fabricated integrated differential operational amplifier is formed from 16 TFTs, whereas TFTs with connected gate and drain contacts are used as load elements. The circuit consists of a differential stage with common mode rejection feedback, a dual to single ended converter, and an additional output stage in a common source amplifier configuration to further boost the amplification. Furthermore, it includes also two current sources to enable circuit operation without external bias voltages. All geometrical parameters are optimized using a SPICE simulation and a customized level 61 transistor model.[58] The performance of the circuit is evaluated by applying a supply voltage of 5 V, and two differential sinusoidal input signals with an AC amplitude of 100 mV and a DC offset of 2.3 V, while a total load of 1 MΩ and 2 pF was connected to the output. Under these conditions, the operational amplifier consumes 950 μW and exhibits a voltage gain of 19.1 dB, a −3 dB frequency of 109 kHz, and a unity gain frequency of 495 kHz, resulting in a gain-bandwidth product of 4.46 MHz. The common mode rejection is ≈44 dB in the linear gain regime and 16 dB at the unity gain frequency.

Characterization of the Mechanical Properties of the IGZO Devices: The flexibility of TFTs and circuits on polyimide foil was evaluated by winding the devices around rods with different diameters using double sided tape. This induced tensile mechanical strain into the device layers. The presented TFTs were tested while flat and bend to radii of 10, 5, and 3.5 mm, which corresponds to stain values of 0%, 0.2%, 0.5%, and 0.7% parallel to the TFT channel.[81] The TFTs stay fully operational while bent and exhibit in average only small parameter changes such as a threshold voltage reduction of −25 mV and an increase of the effective mobility by 1%. A maximum gate leakage current of 10 pA independent of the bending state confirms the intactness of the gate insulator (Figure 2a). Bending the device perpendicular to the TFT channel causes smaller parameter change but can also lead to unpredictable formation of capillary cracks.[60]

The complete amplifier is also tested under bending. Since all TFTs within the circuit are aligned parallel to each other, tensile strain of 0.5% is induced parallel to all TFT channels at the same time. While all other measurement conditions are kept unchanged as in the discussion above, a voltage gain of 18.9 dB, a −3 dB frequency of 113 kHz, a unity gain frequency of 508 kHz, and therefore a gain-bandwidth product of 4.48 MHz are extracted (Figure 2b). This small increase mirrors the slight performance improvement (increased mobility) of single TFTs under tensile strain. The common mode rejection is not affected by bending.

Integrated Magnetosensitive Device: All flexible amplifiers (22 per 76 × 76 mm^2 substrate) were prepared in a single process on a 50 μm thick polyimide foil. Amplifiers were precharacterized in a probe station by applying power and input signals from an external supply. Electrical excitation of the amplifier was performed by an external two-channel function generator connected to the differential input terminals of the amplifier circuit while the output signals were acquired using a multichannel oscilloscope.

The noise characterization was performed at room temperature using an external spectrum analyzer by acquiring the noise spectral density at the outputs of the operational amplifier and the power amplifier in a powered (3 V) state with a 50 Ω load resistor. Here the bandwidth of the spectrum analyzer was set to 1 kHz. The noise acquisition was done with a shunting 50 Ω resistor attached between the differential inputs of the amplifier and 1.5 V bias. The SNR was measured by applying a ±10 μV differential sinusoidal signal on a loaded input of the amplifier with 1.5 V bias. The amplifier sensitivity has been determined with respect to the 50 Ω shunt resistor and normalized for the spectral resolution of our spectrum analyzer, whereas the reference was the measured SNR of 56 dB.

After the characterization, readout circuits were separated into single devices by cutting the substrate with regular office scissors. Separated devices were temporarily attached to glass substrates for further processing. Readout circuits with acceptable characteristics were passivated with a layer of polychloroprene, and a GMR bridge connected to the operational amplifier was fabricated. Then the complete circuit was electrically contacted in a probe station for characterisation and testing purposes with and without external magnetic fields. For the switching and proximity demonstration, the flexible magnetosensory system was combined with an additional flexible circuit consisting of an IGZO TFT and a commercial semiconductor light emitting diode (EOLC-660-23-1 EPIGAP Optronic GmbH, Germany) connected in series with the TFT using printed silver conductors. The LED circuit was fixed in a probe station and supplied with 3 V using an external power supply.

Supporting Information

Supporting Information is available from the Wiley Online Library or from the author.

Acknowledgements

N.M. and D.K. contributed equally to this work. The authors thank C. Krien and I. Fiering (IFW Dresden) for the deposition of the magnetic sensor bridge as well as C. Zysset for help in circuit design and characterization. The support in the development of the experimental setups from the research technology department of the IFW Dresden and the clean room team headed by Dr. S. Harazim (IFW Dresden) is greatly appreciated. This work was financed in part via the European Research Council (ERC) within the European Union´s Seventh Framework Programme (FP7/2007-2013)/ERC Grant Agreement No. 306277 and European Commission within the European Union´s seventh framework program FLEXIBILITY/Grant No. 287568.

Received: May 5, 2016
Published online: June 27, 2016

[1] D. H. Kim, J. A. Rogers, *Adv. Mater.* **2008**, *20*, 4887.
[2] K. Nomura, H. Ohta, A. Takagi, T. Kamiya, M. Hirano, H. Hosono, *Nature* **2004**, *432*, 488.
[3] S. Park, M. Vosguerichian, Z. Bao, *Nanoscale* **2013**, *5*, 1727.
[4] S. Wagner, S. Bauer, *MRS Bull.* **2012**, *37*, 207.
[5] G. A. Salvatore, N. Münzenrieder, T. Kinkeldei, L. Petti, C. Zysset, I. Strebel, L. Büthe, G. Tröster, *Nat. Commun.* **2014**, *5*, 2982.
[6] M.-G. Kim, M. G. Kanatzidis, A. Facchetti, T. J. Marks, *Nat. Mater.* **2011**, *10*, 382.

[7] J. Viventi, D.-H. Kim, L. Vigeland, E. S. Frechette, J. A. Blanco, Y.-S. Kim, A. E. Avrin, V. R. Tiruvadi, S.-W. Hwang, A. C. Vanleer, D. F. Wulsin, K. Davis, C. E. Gelber, L. Palmer, J. Van der Spiegel, J. Wu, J. Xiao, Y. Huang, D. Contreras, J. A. Rogers, B. Litt, *Nat. Neurosci.* **2011**, *14*, 1599.
[8] T. Sekitani, U. Zschieschang, H. Klauk, T. Someya, *Nat. Mater.* **2010**, *9*, 1015.
[9] I. D. Joshipura, H. R. Ayers, C. Majidi, M. D. Dickey, *J. Mater. Chem. C* **2015**, *3*, 3834.
[10] C. Hunger, K. D. M. Rao, R. Gupta, C. R. Singh, G. U. Kulkarni, M. Thelakkat, *Energy Technol.* **2015**, *3*, 638.
[11] M. Kaltenbrunner, M. S. White, E. D. Głowacki, T. Sekitani, T. Someya, N. S. Sariciftci, S. Bauer, *Nat. Commun.* **2012**, *3*, 770.
[12] D. Karnaushenko, B. Ibarlucea, S. Lee, G. Lin, L. Baraban, S. Pregl, M. Melzer, D. Makarov, W. M. Weber, T. Mikolajick, O. G. Schmidt, G. Cuniberti, *Adv. Healthcare Mater.* **2015**, *4*, 1517.
[13] S. S. Ehrmeyer, R. H. Laessig, *Clin. Chem. Lab. Med.* **2007**, *45*, 766.
[14] Y.-H. Lao, K. Peck, L.-C. Chen, *Anal. Chem.* **2009**, *81*, 1747.
[15] D. Karnaushenko, L. Baraban, D. Ye, I. Uguz, R. G. Mendes, M. H. Rümmeli, J. A. G. M. de Visser, O. G. Schmidt, G. Cuniberti, D. Makarov, *Sci. Rep.* **2015**, *5*, 12878.
[16] Y. Sun, J. A. Rogers, *Adv. Mater.* **2007**, *19*, 1897.
[17] L. Li, Q. Ling, S. Lim, Y. Tan, C. Zhu, D. S. H. Chan, E. Kang, K. Neoh, *Org. Electron.* **2007**, *8*, 401.
[18] L. Petti, N. Munzenrieder, G. A. Salvatore, C. Zysset, T. Kinkeldei, L. Buthe, G. Troster, *IEEE Trans. Electron Devices* **2014**, *61*, 1085.
[19] B. Li, M. N. Kavaldzhiev, J. Kosel, *J. Magn. Magn. Mater.* **2015**, *378*, 499.
[20] H. Liu, M. Li, O. Voznyy, L. Hu, Q. Fu, D. Zhou, Z. Xia, E. H. Sargent, J. Tang, *Adv. Mater.* **2014**, *26*, 2718.
[21] G. Gustafsson, Y. Cao, G. M. Treacy, F. Klavetter, N. Colaneri, A. J. Heeger, *Nature* **1992**, *357*, 477.
[22] M. Melzer, J. I. Mönch, D. Makarov, Y. Zabila, G. S. C. Bermúdez, D. Karnaushenko, S. Baunack, F. Bahr, C. Yan, M. Kaltenbrunner, O. G. Schmidt, *Adv. Mater.* **2015**, *27*, 1274.
[23] D. Karnaushenko, N. Münzenrieder, D. D. Karnaushenko, B. Koch, A. K. Meyer, S. Baunack, L. Petti, G. Tröster, D. Makarov, O. G. Schmidt, *Adv. Mater.* **2015**, *27*, 6797.
[24] D. Makarov, M. Melzer, D. Karnaushenko, O. G. Schmidt, *Appl. Phys. Rev.* **2016**, *3*, 011101.
[25] M. Melzer, M. Kaltenbrunner, D. Makarov, D. Karnaushenko, D. Karnaushenko, T. Sekitani, T. Someya, O. G. Schmidt, *Nat. Commun.* **2015**, *6*, 6080.
[26] M. Kaltenbrunner, T. Sekitani, J. Reeder, T. Yokota, K. Kuribara, T. Tokuhara, M. Drack, R. Schwödiauer, I. Graz, S. Bauer-Gogonea, S. Bauer, T. Someya, *Nature* **2013**, *499*, 458.
[27] D. Khodagholy, J. N. Gelinas, T. Thesen, W. Doyle, O. Devinsky, G. G. Malliaras, G. Buzsáki, *Nat. Neurosci.* **2014**, *18*, 310.
[28] L. Xu, S. R. Gutbrod, A. P. Bonifas, Y. Su, M. S. Sulkin, N. Lu, H.-J. Chung, K.-I. Jang, Z. Liu, M. Ying, C. Lu, R. C. Webb, J.-S. Kim, J. I. Laughner, H. Cheng, Y. Liu, A. Ameen, J.-W. Jeong, G.-T. Kim, Y. Huang, I. R. Efimov, J. A. Rogers, *Nat. Commun.* **2014**, *5*, 3329.
[29] S. Gong, W. Schwalb, Y. Wang, Y. Chen, Y. Tang, J. Si, B. Shirinzadeh, W. Cheng, *Nat. Commun.* **2014**, *5*, 3132.
[30] A. Chortos, Z. Bao, *Mater. Today* **2014**, *17*, 321.
[31] T. Yokota, T. Sekitani, T. Tokuhara, N. Take, U. Zschieschang, H. Klauk, K. Takimiya, T. Huang, M. Takamiya, T. Sakurai, T. Someya, *IEEE Trans. Electron Devices* **2012**, *59*, 3434.
[32] G. Lin, D. Makarov, M. Melzer, W. Si, C. Yan, O. G. Schmidt, *Lab Chip* **2014**, *14*, 4050.
[33] M. Melzer, D. Makarov, A. Calvimontes, D. Karnaushenko, S. Baunack, R. Kaltofen, Y. Mei, O. G. Schmidt, *Nano Lett.* **2011**, *11*, 2522.
[34] K. Ishida, R. Shabanpour, B. Kheradmand-Boroujeni, T. Meister, C. Carta, F. Ellinger, L. Petti, N. S. Munzenrieder, G. A. Salvatore, G. Troster, in *2014 IEEE Asian Solid-State Circuits Conf.*, KaoHsiung, IEEE, **2014**, pp. 313–316.
[35] R. Shabanpour, T. Meister, K. Ishida, L. Petti, N. Münzenrieder, G. A. Salvatore, B. Kheradmand-Boroujenii, C. Carta, G. Tröster, F. Ellinger, in *21st IEEE Int. Conf. Electron. Circuits Syst.*, Marseille, IEEE, **2014**, pp. 108–111.
[36] H. Klauk, U. Zschieschang, J. Pflaum, M. Halik, *Nature* **2007**, *445*, 745.
[37] M. Takamiya, H. Fuketa, K. Ishida, T. Yokota, T. Sekitani, T. Someya, T. Sakurai, in *57th IEEE Int. Midwest Symp. Circuits Syst.*, College Station, TX, IEEE, **2014**, pp. 829–832.
[38] W. Zeng, L. Shu, Q. Li, S. Chen, F. Wang, X.-M. Tao, *Adv. Mater.* **2014**, *26*, 5310.
[39] M.-C. Lin, M. Gong, B. Lu, Y. Wu, D.-Y. Wang, M. Guan, M. Angell, C. Chen, J. Yang, B.-J. Hwang, H. Dai, *Nature* **2015**, *520*, 324.
[40] E. Madej, M. Espig, R. R. Baumann, W. Schuhmann, F. La Mantia, *J. Power Sources* **2014**, *261*, 356.
[41] C. Dagdeviren, B. D. Yang, Y. Su, P. L. Tran, P. Joe, E. Anderson, J. Xia, V. Doraiswamy, B. Dehdashti, X. Feng, B. Lu, R. Poston, Z. Khalpey, R. Ghaffari, Y. Huang, M. J. Slepian, J. A. Rogers, *Proc. Natl. Acad. Sci. USA* **2014**, *111*, 1927.
[42] R. Kwok, *Nature* **2013**, *497*, 176.
[43] S. S. Bhatlawande, J. Mukhopadhyay, M. Mahadevappa, in *2012 Natl. Conf. Commun.*, Kharagpur, IEEE, **2012**, pp. 1–4.
[44] L. Dunai, B. D. Garcia, I. Lengua, G. Peris-Fajarnes, in *IECON 2012 – 38th Annu. Conf. IEEE Ind. Electron. Soc.*, Montreal, QC, IEEE, **2012**, pp. 4208–4215.
[45] D.-H. Kim, S. Wang, H. Keum, R. Ghaffari, Y.-S. Kim, H. Tao, B. Panilaitis, M. Li, Z. Kang, F. Omenetto, Y. Huang, J. A. Rogers, *Small* **2012**, *8*, 3263.
[46] G. Di Pino, A. Benvenuto, G. Cavallo, L. Denaro, V. Denaro, F. Ferreri, L. Rossini, M. Tombini, D. Accoto, M. C. Carrozza, S. Micera, E. Guglielmelli, P. M. Rossini, in *Grasping the Future: Advances in Powered Upper Limb Prosthetics*, Bentham Science, Beijing, **2012**, pp. 28–38.
[47] N. Lu, D.-H. Kim, *Soft Robot.* **2014**, *1*, 53.
[48] R. H. Baughman, *Synth. Met.* **1996**, *78*, 339.
[49] E. Palleau, D. Morales, M. D. Dickey, O. D. Velev, *Nat. Commun.* **2013**, *4*, 2257.
[50] R. Yoshida, T. Ueki, *NPG Asia Mater.* **2014**, *6*, e107.
[51] NVE Corporation; GMR sensor AA002-02, <www.nve.com/Downloads/analog_catalog.pdf>, accessed October 2015.
[52] Sensitec GmbH, GMR sensor AFF755B, <http://sensitec.com/upload/SENSITEC/PDF_Downloads/Datenblatt/Sensitec_AFF755B_DSE_03.pdf>, accessed October 2015.
[53] Texas Instruments, Hall effect sensor DRV5053VA, <www.ti.com/lit/ds/symlink/drv5053.pdf>, accessed October 2015.
[54] Aichi Micro Intel. Cor., GMI sensor MI-CB-1DH, <http://www.aichi-mi.com/e-home/highly-sensitive-magnetometers/type-dh/>, accessed October 2015.
[55] Quantum Design, SQUID-VSM MPMS, <http://qdusa.com/products/mpms.html>, accessed October 2015.
[56] D. Karnaushenko, D. D. Karnaushenko, D. Makarov, S. Baunack, R. Schäfer, O. G. Schmidt, *Adv. Mater.* **2015**, *27*, 6582.
[57] D. Karnaushenko, D. Makarov, M. Stöber, D. D. Karnaushenko, S. Baunack, O. G. Schmidt, *Adv. Mater.* **2015**, *27*, 880.
[58] C. Zysset, N. Munzenrieder, L. Petti, L. Buthe, G. A. Salvatore, G. Troster, *IEEE Electron Device Lett.* **2013**, *34*, 1394.
[59] N. Münzenrieder, G. Cantarella, C. Vogt, L. Petti, L. Büthe, G. A. Salvatore, Y. Fang, R. Andri, Y. Lam, R. Libanori, D. Widner, A. R. Studart, G. Tröster, *Adv. Electron. Mater.* **2015**, *1*, 1400038.
[60] N. Münzenrieder, C. Zysset, T. Kinkeldei, G. Tröster, *IEEE Trans. Electron Devices* **2012**, *59*, 2153.
[61] T. Yamamoto, T. Takei, Y. Nakajima, Y. Fujisaki, T. Furukawa, M. Hosoi, A. Kinoshita, H. Fujikake, *IEEE Trans. Ind. Appl.* **2012**, *48*, 1662.

ADVANCED ELECTRONIC MATERIALS
www.advelectronicmat.de

[62] N. Münzenrieder, G. A. Salvatore, L. Petti, C. Zysset, L. Büthe, C. Vogt, G. Cantarella, G. Tröster, *Appl. Phys. Lett.* **2014**, *105*, 263504.
[63] Y. C. Tarn, P. C. Ku, H. H. Hsieh, L. H. Lu, *IEEE J. Solid-State Circuits* **2010**, *45*, 1028.
[64] F. Ante, D. Kälblein, T. Zaki, U. Zschieschang, K. Takimiya, M. Ikeda, T. Sekitani, T. Someya, J. N. Burghartz, K. Kern, H. Klauk, *Small* **2012**, *8*, 73.
[65] H. Marien, M. Steyaert, N. Aerle, P. Heremans, in *IEEE Int. Solid-State Circuits Conf.*, San Francisco, CA, IEEE, **2010**, pp. 136–137.
[66] K. Myny, S. Winckel, S. Steudel, P. Vicca, S. De Jonge, M. J. Beenhakkers, C. W. Sele, N. A. J. M. Aerle, G. H. Gelinck, J. Genoe, P. Heremans, in *Dig. Tech. Pap. – IEEE Int. Solid-State Circuits Conf.*, San Francisco, CA, IEEE, **2008**, pp. 298–300.
[67] S. S. P. Parkin, *Annu. Rev. Mater. Sci.* **1995**, *25*, 357.
[68] M. Melzer, D. Karnaushenko, G. Lin, S. Baunack, D. Makarov, O. G. Schmidt, *Adv. Mater.* **2015**, *27*, 1333.
[69] Y. Chen, Y. Mei, A. Malachias, J. I. Moench, R. Kaltofen, O. G. Schmidt, *J. Phys. Condens. Matter* **2008**, *20*, 452202.
[70] H. Marien, M. S. J. Steyaert, E. Veenendaal, P. Heremans, *IEEE J. Solid-State Circuits* **2012**, *47*, 1712.
[71] R. Shabanpour, K. Ishida, T. Meister, N. Münzenrieder, L. Petti, G. Salvatore, B. Kheradmand-Boroujeni, C. Carta, G. Tröster, F. Ellinger, in *2015 IEEE 58th Int. Midwest Symp. Circuits Syst.*, Fort Collins, CO, IEEE, **2015**, pp. 1–4.
[72] R. Shabanpour, C. Carta, T. Meister, K. Ishida, B. Kherdmand-Boroujeni, F. Ellinger, N. Münzenrieder, G. Salvatore, L. Petti, G. Tröster, in *2015 European Conference on Circuit Theory and Design (ECCTD)*, Trondheim, IEEE, **2015**, 1–4.
[73] J.-H. Ahn, H.-S. Kim, E. Menard, K. J. Lee, Z. Zhu, D.-H. Kim, R. G. Nuzzo, J. A. Rogers, I. Amlani, V. Kushner, S. G. Thomas, T. Duenas, *Appl. Phys. Lett.* **2007**, *90*, 213501.
[74] Y. Chen, Y. Mei, R. Kaltofen, J. I. Mönch, J. Schumann, J. Freudenberger, H.-J. Klauß, O. G. Schmidt, *Adv. Mater.* **2008**, *20*, 3224.
[75] D. Karnaushenko, D. Makarov, C. Yan, R. Streubel, O. G. Schmidt, *Adv. Mater.* **2012**, *24*, 4518.
[76] D. Makarov, D. Karnaushenko, O. G. Schmidt, *ChemPhysChem* **2013**, *14*, 1771.
[77] A. A. Stokes, R. F. Shepherd, S. a. Morin, F. Ilievski, G. M. Whitesides, *Soft Robot.* **2014**, *1*, 70.
[78] F. Ilievski, A. D. Mazzeo, R. F. Shepherd, X. Chen, G. M. Whitesides, *Angew. Chem., Int. Ed.* **2011**, *50*, 1890.
[79] R. V. Martinez, A. C. Glavan, C. Keplinger, A. I. Oyetibo, G. M. Whitesides, *Adv. Funct. Mater.* **2014**, *24*, 3003.
[80] N. Pérez, M. Melzer, D. Makarov, O. Ueberschär, R. Ecke, S. E. Schulz, O. G. Schmidt, *Appl. Phys. Lett.* **2015**, *106*, 153501.
[81] H. Gleskova, I. C. Cheng, S. Wagner, J. C. Sturm, Z. Suo, *Sol. Energy* **2006**, *80*, 687.